Dalton Transactions

ROYAL SOCIETY OF CHEMISTRY

PAPER

View Article Online
View Journal | View Issue

Cite this: *Dalton Trans.*, 2025, **54**, 16727

Stability, structure, dynamics and thermal properties of C-type aluminium tris-dihydrogen phosphate

Sheyi C. Adediwura,[a] Jan K. Wied,[a] Christian F. Litterscheid[b] and Jörn Schmedt auf der Günne *[a]

Received 6th September 2025,
Accepted 23rd September 2025

DOI: 10.1039/d5dt02141c

rsc.li/dalton

Among the fastest hydrogen ion conductors are various hydrogen-rich phosphates, such as phosphoric acid and CsH_2PO_4. This, in principle, makes $Al(H_2PO_4)_3$ a promising candidate for proton conduction within its hydrogen bonding network, especially in the medium-temperature range. Here, the phase-pure synthesis and structural details of the ferroelectric crystal C-type $Al(H_2PO_4)_3$ are reported, where density functional theory (DFT) calculations were used to study the thermodynamic stability of different Al $(H_2PO_4)_3$ polymorphs. Its ion conductivity, as determined by impedance spectroscopy, is an order of magnitude higher than previously reported. The thermal stability and decomposition route of $Al(H_2PO_4)_3$ were studied using XRD, thermal analysis, and solid-state NMR, yielding results different from those previously observed in various mixtures containing $Al(H_2PO_4)_3$. Heating produces an amorphous intermediate phase which converts into phase-pure monoclinic $Al_2(P_6O_{18})$, which at even higher temperatures converts into the cubic phase $Al_4(P_4O_{12})_3$ and little $AlPO_4$. Rietveld refinements of C-type $Al(H_2PO_4)_3$ and $Al_4(P_4O_{12})_3$ are provided. The results show that while the proton ion conductivity of C-type $Al(H_2PO_4)_3$ is hampered by the strong hydrogen-bonds, the structure features a Curie temperature significantly higher than room-temperature.

Introduction

Aluminium phosphates are essential in refractories and thermal spray coatings, largely due to their excellent physical, chemical, and mechanical properties.[1,2] The strong binding properties of phosphate binders are linked to their inherent phosphate bonds, which enhance strength, thermal stability, and resistance to abrasion.[3–7] Among these, $Al(H_2PO_4)_3$ is particularly effective due to its high solubility in water and its ability to achieve significant initial strength.[5,7,8] Beyond its binding role, $Al(H_2PO_4)_3$ exhibits proton conduction behaviour similar to *ortho*-phosphoric acid, a common electrolyte in phosphoric acid fuel cells.[9,10] The 85% H_3PO_4 serves as a liquid electrolyte with high proton conductivity,[9,11] while pure H_3PO_4 is a room-temperature solid (melting point: 42 °C). Both forms are hygroscopic. CsH_2PO_4 exhibits similarly high proton conductivity in its superprotonic phase.[9] Like H_3PO_4 and CsH_2PO_4, $Al(H_2PO_4)_3$ is highly hygroscopic[2,12,13] and readily forms various hydrates.[14] Its PO_4 group enables hydrogen-bonded networks that facilitate proton transfer between phosphate units,[9] suggesting its potential as an electrolyte in intermediate-temperature fuel cells.

$Al(H_2PO_4)_3$ is typically synthesised through the reaction of *ortho*-phosphoric acid H_3PO_4 with aluminium oxide, aluminium hydroxide, or elemental aluminium.[12,13,15–17,18] To date, four polymorphs *i.e.*, A-, B-, C-, and D-type $Al(H_2PO_4)_3$ have been identified,[15,16] although detailed reports exist only for A-, B-, and C-types.[12,13,18] The A-type forms when an aged solution of aluminium in concentrated phosphoric acid (Al : P = 1 : 5.5) is slowly evaporated under constant temperature conditions.[13] The phase referred to here as "B-type $Al(H_2PO_4)_3$" has only been reported in form of the Fe-substituted Al $(H_2PO_4)_3$ and was prepared under hydrothermal conditions at elevated pressure.[18] The C-type is obtained through the evaporation of viscous solutions of aluminium in concentrated phosphoric acid (Al : P = 1 : 5).[12]

The A-type $Al(H_2PO_4)_3$ adopts a hexagonal crystal structure, with lattice parameters a = 7.858(4) Å and c = 24.956(7) Å (Pearson symbol: $hR56$, space group $R\bar{3}c$).[13,15] It consists of AlO_6 octahedral that share corners with six $PO_2(OH)_2$ tetrahedra, forming a three-dimensional network. The structure of

[a]*University of Siegen, Faculty IV: School of Science and Technology, Department for Chemistry and Biology, Inorganic Materials Chemistry and Center of Micro- and Nanochemistry and (Bio)Technology (Cμ), Adolf-Reichwein Straße 2, 57076 Siegen, Germany. E-mail: gunnej@chemie.uni-siegen.de*
[b]*Chemische Fabrik Budenheim KG, Rheinstrasse 27, 55257 Budenheim, Germany*

B-type $Al(H_2PO_4)_3$ was derived by removing the Fe/Al disorder (Pearson symbol: *mC*88, space group *Cc*),[18] and its simulated XRD-pattern shows good agreement with the XRD pattern of B-type $Fe(H_2PO_4)_3$. This Fe-substituted form exhibits a distorted sheet-like network linked by M–O–P bridges (M = Fe, Al). The C-type $Al(H_2PO_4)_3$ also crystallises in a hexagonal structure, with lattice parameters a = 13.727(5) Å and c = 9.152 (1) Å (Pearson symbol: *hR*44, space group *R*3*c*)[12] but features AlO_6 octahedral that are stacked and linked by $PO_2(OH)_2$ tetrahedra group in a chain-like arrangement. To the best of our knowledge, its complete crystal structure has not been reported; only lattice parameters, space group and structural images have been provided. Among these $Al(H_2PO_4)_3$ polymorphs, the thermodynamically most stable phase remains unknown. This can be addressed by comparing ground-state energies computed by first-principle methods at various pressures.[19,20]

Obtaining phase-pure $Al(H_2PO_4)_3$ for property characterisation is challenging. This is due to the retention of residual *ortho*-phosphoric acid in the synthesis mixture, which is difficult to fully separate from the product and affects both thermal stability[12] and evolution.[2,17,21–24] A convenient tool to study products is NMR, being intrinsically quantitative and element-specific to P, H and Al, while it allows for monitoring all occurring products, including liquid, crystalline and amorphous constituents, which has also been noted in previous studies about the thermal decomposition of samples containing $Al(H_2PO_4)_3$.[17,21–24] Unfortunately, its thermal evolution is not clear, but different condensation and calcination reactions and temperatures have been suggested. Some studies indicate that C-type $Al(H_2PO_4)_3$ remains stable up to 473 K before transitioning to crystalline $AlH_2P_3O_{10}$ below 623 K.[17,22] Other reports describe the formation of an amorphous "$AlH_2P_3O_{10}$" phase between 473 K and 632 K.[2,17,23] At temperatures above 723 K, two aluminium metaphosphate phases, the monoclinic $Al_2(P_6O_{18})$ and the cubic $Al_4(P_4O_{12})_3$, have been observed.[2,17,22–24] Between 773 K and 873 K, a mixture of these phases is typically observed, with $Al_4(P_4O_{12})_3$ becoming dominant beyond 873 K,[17,22–24] suggesting that $Al_2(P_6O_{18})$ may be metastable.[24] The cubic phase, $Al_4(P_4O_{12})_3$, subsequently decomposes into $AlPO_4$ *via* the elimination of P_4O_{10} at 1473 K, before transitioning into an amorphous phase beyond 1673 K.[2,17,21–24] It should be noted that in those cases where NMR spectra were reported[17,22–24] the samples were not single-phase C-type $Al(H_2PO_4)_3$ but always contained different amounts of *ortho*-phosphoric acid and its condensation products. In a similar way, the ionic conductivity of pure C-type $Al(H_2PO_4)_3$ has not been characterised yet, but only mixtures of C-type $Al(H_2PO_4)_3$ and H_3PO_4.[25] While existing research offers valuable insights into the thermal and conductive properties of C-type $Al(H_2PO_4)_3$, discrepancies and unresolved questions highlight the need for further investigation into how impurities affect its thermal stability, phase transitions, and ionic conductivity.

The target of this contribution is to get a better understanding of $Al(H_2PO_4)_3$ starting from phase-pure C-type $Al(H_2PO_4)_3$, the stability of its different polymorphs, its ionic conductivity and thermal decomposition.

Experimental part

Synthesis of $Al(H_2PO_4)_3$

552 mg of Al powder was filed off from an Al bar with a rasp inside a glove box (MBraun, Garching, Germany) under an argon atmosphere. It was dissolved in 24.04 g of 85% H_3PO_4 (purity ≥99.9%, Carl Roth, Germany) at a ratio of 1 : 4, following eqn (1), under a constant N_2 gas flow, at 333 K with a constant stirring rate of 6.7 Hz. Once the aluminium powder had fully dissolved in concentrated phosphoric acid, the solution was heated at 378 K for 24 hours to remove water and partially condense the phosphoric acid. The resulting mixture was then washed with acetonitrile to remove excess phosphoric acid and subsequently dried under vacuum (~1.0×10^{-2} mbar). Its thermal evolution was analysed through calcination in air at different temperatures: 573 K for 3 hours, 623 K for 6 hours, 823 K for 12 hours, 1123 K for 24 hours, and 1273 K for 12 hours.

$$2Al + 6H_3PO_4 \rightarrow 2Al(H_2PO_4)_3 + 3H_2 \uparrow \quad (1)$$

Powder X-ray diffraction

X-ray powder diffraction (XRD) patterns were obtained using two diffractometers. The first, a STOE STADI P powder diffractometer (Stoe, Darmstadt, Germany), operated with Ge(111)-monochromated Cu $K\alpha_1$ radiation (λ = 1.54056 Å) in Debye–Scherrer geometry. The powder samples were finely ground and packed into capillaries with an inner diameter of 0.48 mm. Data collection was performed with a linear position-sensitive detector over a 2θ range of 5° to 90°, with a step size of 0.015° and a counting time of 180 s per step.

The second diffractometer used was a Huber Guinier powder camera G621 (Huber, Rimsting, Germany), configured in asymmetric transmission geometry. A curved Ge(111) monochromator was used to focus and monochromatise the X-ray beam, isolating Cu $K\alpha_1$ radiation. Samples were prepared by evenly spreading the powder onto 1 μm thick Mylar foil affixed to a circular metallic sample holder using a small amount of grease for stabilisation. During measurements, the samples were laterally translated within the X-ray beam to ensure uniform exposure. Diffraction patterns were recorded on BaFX: Eu-based imaging plate (IP) film, with an exposure time of 15 minutes. The exposed imaging plates were subsequently scanned using a Typhoon FLA 7000 scanner (GE Company, USA), and the diffraction images were digitised using IPreader software.[26]

Structural refinements were performed using the TOPAS academic software package (v 7.24).[27] Pawley[28] and Rietveld[29] refinement techniques were applied. The refinement parameters included: the scale factor and background coefficients, modelled using a Chebyshev function (10–14 free parameters), peak shape determined using the fundamental parameter

approach, zero-shift corrections, lattice constants. For Rietveld refinements, hydrogen atom positions were constrained using distance restraints, while other atomic positions were refined considering site symmetry according to the space group. The quality of the structural models was assessed using fit indicators, including R_p (profile R-factor), R_{wp} (weighted profile R-factor), and R_{exp} (expected R-factor).

Nuclear magnetic resonance

All 1D (^{1}H, ^{31}P and ^{27}Al) and 2D (^{31}P–^{31}P) double quantum MAS solid-state NMR experiments were performed at 14.1 T on a Bruker Avance Neo NMR spectrometer equipped with a commercial 3.2 mm MAS probe head at a frequency of 600.2 MHz, 242.9 MHz and 156.4 MHz for ^{1}H, ^{31}P and ^{27}Al, respectively, with a MAS rate of 20 kHz. The chemical shift values of ^{31}P and ^{27}Al are reported on a de-shielding scale, relative to an 85% solution of H_3PO_4 and a solution of 1.1 M $Al(NO_3)_3$ in D_2O, respectively. The ^{1}H resonance of 1% TMS in $CDCl_3$ served as an external secondary reference using the Ξ values for ^{31}P and ^{27}Al as reported by IUPAC.[30,31]

The nutation for ^{1}H, ^{31}P and ^{27}Al were 90.91 kHz, 83.33 kHz and 62.50 kHz, respectively, corresponding to 90° pulse durations of 2.75 μs, 3 μs and 4 μs, respectively. The 1D ^{1}H, ^{31}P and ^{27}Al MAS NMR spectra were recorded using a recycle delay of $5T_1$ and the dead time delay of 6 μs. 2D ^{31}P–^{31}P double-quantum MAS NMR spectra and ^{31}P double-quantum build-up curves were recorded using the symmetry-based recoupling sequence $R14_4^5$ (ref. 32) with 560 R elements (*i.e.*, $R = (90_0 - 270_{180})$) and a 16-step phase cycle for the receiver phase to enable $0 \rightarrow \pm2 \rightarrow 0 \rightarrow -1$ coherence pathway.

The Deconv2Dxy[33] program was used for deconvolution of the NMR spectra. The isotropic chemical shift δ_{iso}, the anisotropic chemical shift δ_{aniso}, and the asymmetry parameter η for the ^{31}P NMR spectra, along with the quadrupole coupling constant C_Q and the quadrupolar asymmetry parameter η_Q for the ^{27}Al NMR spectra,[31] were extracted from the ^{31}P and ^{27}Al NMR spectra acquired at spinning frequencies of 4 kHz and 6 kHz, respectively. Their values were obtained by fitting the experimental spectra using the SIMPSON[34,35] package v4.2.1 together with home-written scripts.

Electrochemical impedance spectroscopy

The C-type $Al(H_2PO_4)_3$ powder sample was thoroughly ground in an agate mortar and pressed into a cylindrical pellet (diameter d = 8 mm) between two gold foils as electrical contact, while applying a load of 5 tonnes (equivalent to p = 981.0 MPa) for 20 minutes. The thickness (0.75 mm) of the pellet was measured with an electronic micrometer screw gauge. All preparatory steps were carried out inside a glove box (MBraun, Garching, Germany) under argon atmosphere.

Electrochemical impedance spectroscopy (EIS) measurements were recorded using NEISYS electrochemical impedance analyser (Novocontrol Technologies, Montabaur, Germany) in a home-built cell, which was calibrated before actual measurements based on short/load calibration standards with a 100 Ω resistor as the load. The impedance measurements were recorded in potentiostatic mode, with an amplitude of 7.1 mV_{rms}, in a frequency range from 1 MHz to 50 mHz. The temperature was controlled using a variable temperature and flow controller (NMR Service GmbH) with a constant nitrogen gas flow. Each temperature point was held for 20 minutes to ensure thermal equilibrium with an accuracy of ±0.1 K throughout the EIS measurement. The data analysis was performed using a home-written Python script.[36]

Thermal analysis

Thermogravimetric (TG) and differential thermal analysis (DTA) of the C-type $Al(H_2PO_4)_3$ powder were conducted using a NETZSCH STA 409C/CD instrument. Measurements were carried out under a nitrogen atmosphere, with the temperature ramped from 303 K to 1423 K at a heating rate of 10 K min^{-1}.

Computational chemistry

All density functional theory (DFT) calculations were performed using QUANTUM ESPRESSO v.7.1.[37,38] The computations used the generalised gradient approximation (GGA) with Perdew–Burke–Ernzerhof (PBE)[39] version and van der Waals[40–43] exchange–correlation functionals, used interchangeably. The stability of $Al(H_2PO_4)_3$ polymorphs was investigated by calculating formation energies at different pressures with a variable-cell relaxation approach, using KJPAW[44] pseudopotential and van der Waals[40–43] exchange–correlation functional "vdw-df".

For each compound, the Monkhorst–Pack[45] k-point mesh and energy cutoff were optimised separately. The energy cutoff varied by system, with 120 Ry (1633 eV) applied to specific calculations. The k-point mesh ranged from 4 × 4 × 4 to 10 × 10 × 10 based on convergence tests. The convergence threshold for self-consistency of the electronic wave function was set to 10^{-14} a.u., while the threshold for the total energy and atomic forces were set to 10^{-12} a.u., and 10^{-11} a.u., respectively. All pseudopotentials were taken from pslibrary v1.0,[46] while cif2cell v.2.0 [47] was used to convert all the crystallographic files into input files.

Results and discussion

This study investigates the thermodynamic stability, synthesis and characterisation of $Al(H_2PO_4)_3$, focusing on its structure, thermal decomposition behaviour and proton conductivity. Its structure is studied using solid-state NMR and X-ray diffraction. Proton dynamics are studied by impedance spectroscopy and static ^{1}H NMR on a powder sample. Thermal evolution studies explore the stability range and decomposition products of phase-pure C-type $Al(H_2PO_4)_3$.

Thermodynamic stability of $Al(H_2PO_4)_3$ polymorphs

Density functional theory (DFT) calculations, involving variable-cell relaxation under different cell pressures, were performed on A-, B-, and C-type polymorphs of $Al(H_2PO_4)_3$ to determine the thermodynamically most stable phase. The crys-

tallographic file for A-type $Al(H_2PO_4)_3$ was obtained from the literature.[13] The file for B-type $Al(H_2PO_4)_3$ was derived from $(Fe_{0.81}Al_{0.19})(H_2PO_4)_3$ [18] by substituting Fe with Al. The crystallographic file for C-type $Al(H_2PO_4)_3$ was reconstructed based on the stacking arrangement, bond distances, angles, and a figure provided in a previous study.[12]

The polymorph with the lowest ground-state energy, following full relaxation of both atomic positions and lattice parameters to their most energetically favourable configuration under ambient pressure, is identified as the most stable form of $Al(H_2PO_4)_3$. As shown in Fig. 1, C-type $Al(H_2PO_4)_3$ exhibits the highest stability at standard conditions with the lowest formation energy. This observation explains why C-type Al $(H_2PO_4)_3$ has been the most commonly synthesised polymorph in previous studies.[12,17,22,25] The results in Fig. 1 also indicate that C-type $Al(H_2PO_4)_3$ may transition to A-type $Al(H_2PO_4)_3$ at approximately 1.43 GPa. Similarly, A-type $Al(H_2PO_4)_3$ is predicted to transform into B-type $Al(H_2PO_4)_3$ at around 34.25 GPa. From the volume–pressure curves, the bulk moduli of A-, B-, and C-type were estimated as 69.6 GPa, 37.9 GPa, and 21.7 GPa, respectively (Table S1 and Fig. S1).

Synthesis and phase characterisation of C-type $Al(H_2PO_4)_3$

The conventional synthesis of $Al(H_2PO_4)_3$ (*i.e.*, from $Al(OH)_3$/Al_2O_3 + H_3PO_4) produces mixtures of C-type $Al(H_2PO_4)_3$ and residual H_3PO_4. To obtain phase-pure C-type $Al(H_2PO_4)_3$, Al powder was reacted with 85% H_3PO_4 for the synthesis. A previous study[12] reported a similar method at 50 °C. An attempt at 50 °C using this approach produced C-type $Al(H_2PO_4)_3$ with significant H_3PO_4 impurity (Fig. S2). Preheating the 85% H_3PO_4 above 50 °C before adding Al powder dissolved only one-third of the powder and left substantial H_3PO_4 impurity. Preheating at 50 °C, adding Al powder, and raising the temperature to below 100 °C still yielded C-type $Al(H_2PO_4)_3$ with a high amount of H_3PO_4 impurity.

Extensive trials showed that dissolving Al powder at 50 °C, then heating the viscous solution to 105 °C for at least 24 hours, followed by precipitation and washing of the product with acetonitrile at least three times, removes excess H_3PO_4 effectively. This method consistently produced phase-pure C-type $Al(H_2PO_4)_3$. Purity was confirmed by ^{31}P, ^{27}Al, and ^{1}H magic-angle spinning (MAS) nuclear magnetic resonance (NMR) spectroscopy (Fig. S3). The ^{31}P MAS NMR spectrum displays a single resonance at −16.1 ppm. The ^{27}Al and ^{1}H NMR spectra show single resonances at −15.3 ppm and 10 ppm, respectively. No impurities in the NMR spectra verify phase-pure C-type $Al(H_2PO_4)_3$ synthesis. Chemical shift tensors for ^{31}P and the quadrupolar coupling constant for ^{27}Al are listed in Tables 1 and 2, respectively.

The powder X-ray diffraction patterns of synthesised Al $(H_2PO_4)_3$ were recorded at room temperature using Debye–Scherrer geometry. Pawley refinement was performed on the powder diffractogram in the *R3c* space group. A surprise were the splittings of the reflections observed in the high-angle region, which are not consistent with the proposed structural model.[12] No supercell reflections in the low-angle regime could be observed or anywhere else. According to NMR the samples are phase pure. Structural relaxation of the presented structural model of the B-type $Al(H_2PO_4)_3$ transformed to the space group *P*1 with quantum-chemical calculations conserves the high symmetry and indicates the structure is at a true energetic minimum. The splittings can be modelled with two unit cells with slightly different lattice parameters with equal intensity (Fig. S7): $a = b$ = 13.6859(1) Å, c = 9.1314(1) Å and $a = b$ = 13.6961(1) Å, c = 9.1402(1) Å, similar to those previously reported.[12,16]

The theoretically generated structure was subsequently used for Rietveld refinement analysis, neglecting the splittings in the high-angle regime by using angles up to 65.5°. The analysis yielded lattice parameters of $a = b$ = 13.6862(1) Å and c =

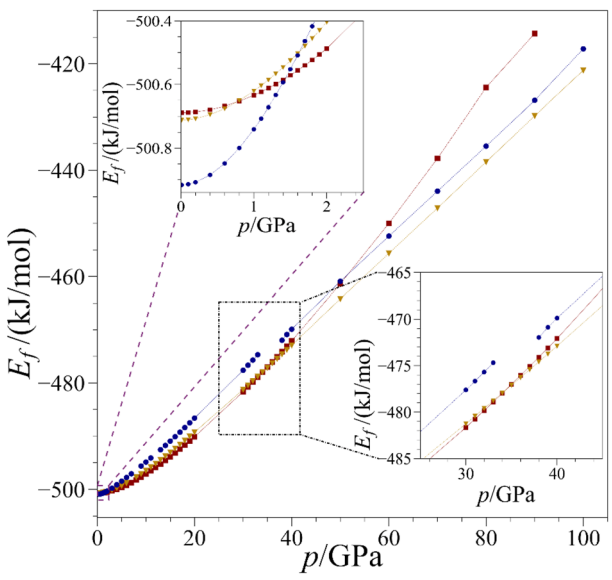

Fig. 1 The plot shows the formation energy E_f per atom at different pressures p during the variable-cell relaxation DFT calculations for A-type $Al(H_2PO_4)_3$ (red squares), B-type $Al(H_2PO_4)_3$ (yellow triangles) and C-type $Al(H_2PO_4)_3$ (blue circles) polymorphs. The insert shows crossover points at 1.4 GPa for the C- to A-type transition (E_f = −500.6 (kJ mol^{-1})) and at 34.3 GPa for A- to B-type transition (E_f = −477.7 (kJ mol^{-1})). The values are subject to a significant error given vibrations are not considered.

Table 1 ^{31}P NMR parameters isotropic chemical shift δ_{iso}, anisotropic chemical shift δ_{aniso}, asymmetry parameter η, principal values δ_{11}, δ_{22} and δ_{33}, for C-type $Al(H_2PO_4)_3$, $Al_2(P_6O_{18})$ and $Al_4(P_4O_{12})_3$ phases as determined by analysis of the experimental NMR data in (Fig. S4–6)

Phase	δ_{iso}/ppm	δ_{aniso}/ppm	η	δ_{11}/ppm	δ_{22}/ppm	δ_{33}/ppm
C-type Al $(H_2PO_4)_3$	−16.1	−64	0.81	42.1	−10.2	−80.2
$Al_2(P_6O_{18})$	−36.6	−105	0.61	48.0	−16.1	−141.6
	−37.5	−107	0.67	51.7	−19.7	−144.8
	−43.3	−110	0.58	43.6	−20.4	−153.1
$Al_4(P_4O_{12})_3$	−50.8	−119	0.41	33.0	−15.5	−169.7
α-$AlPO_4$ (cristobalite)	−26.7	—	—	—	—	—

Table 2 ^{27}Al NMR parameters: isotropic chemical shift δ_{iso}, quadrupolar asymmetry parameter η_Q quadrupolar coupling constant C_Q for C-type $Al(H_2PO_4)_3$, $Al_2(P_6O_{18})$ and $Al_4(P_4O_{12})_3$ phases as determined by analysis of the experimental NMR data in Fig. S4–6

	^{27}Al NMR		
Phase	δ_{iso}^{exp}/ppm	η_Q^{exp}	$\lvert C_Q^{exp}\rvert$/MHz
C-type $Al(H_2PO_4)_3$	−15.3	0	0.88
$Al_2(P_6O_{18})$	−13.2	0.35	1.29
$Al_4(P_4O_{12})_3$	−20.7	0	0.22
α-$AlPO_4$ (cristobalite)	41.5[a]	0.75 (ref. 48)	1.2 (ref. 48)

[a] This work.

9.1333(1) Å, which align well with the Pawley refinement results and prior studies.[12,16] The powder pattern fit (Fig. 2) exhibits strong agreement with the theoretical structure, with minimal deviations observed.

The space group of C-type $Al(H_2PO_4)_3$ belongs to the non-centrosymmetric pyroelectric point group ($3m$).[49] The structure features a polar axis along which the hydrogen-bonds generate a permanent electric-dipole.[49] The presence of a unique polar axis in C-type $Al(H_2PO_4)_3$, as highlighted in an earlier study,[12] suggests that the sample is in a ferroelectric state below its Curie temperature, and a potential transition to the centrosymmetric supergroup $R\bar{3}c$ in the paraelectric phase may occur at higher temperatures. The observed peak splittings in the high-angle regime (Fig. S7) might be related to this material's property, but NMR (number of peaks and NMR parameters) and quantum-chemical results do not give any evidence of a symmetry reduction or different unit cell.

Proton conductivity of C-type $Al(H_2PO_4)_3$

Impedance spectroscopy measurements of C-type $Al(H_2PO_4)_3$ were performed over the temperature range of 373 to 453 K. The complex impedance spectrum at 373 K (Fig. 3) shows a single region, along with evidence of double-layer formation at the sample/electrode interface. The experimental data were modelled using an equivalent circuit (Fig. 3 inset) consisting of a parallel combination of a resistor R_b, a constant-phase element CPE_b and a capacitor C_b. The impedance of the constant-phase element is given by $Z_{CPE} = \frac{1}{Q(i\omega)^{\alpha}}$, with prefactor Q and exponent $\alpha < 1$. In this model, R_b describes the diffusive transport, the CPE_b represents the subdiffusive transport and C_b corresponds to high-frequency polarization (electronic and vibrational). The additional CPE_{el} accounts for the non-ideal double-layer formation at the electrode interface.

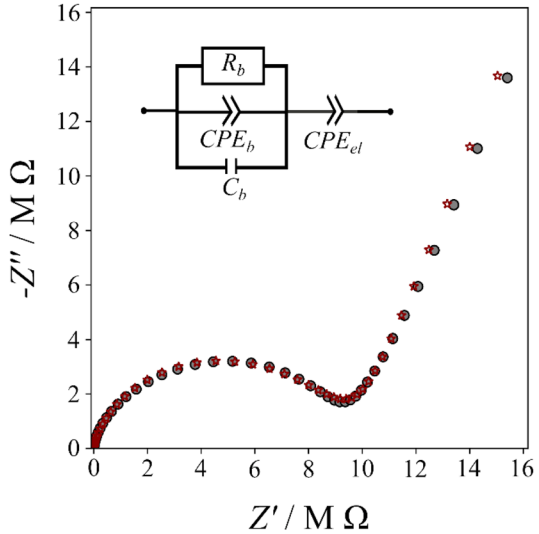

Fig. 3 Nyquist (imaginary part of the impedance against real part) plot of impedance measurements of C-type $Al(H_2PO_4)_3$. Pellet (diameter = 8 mm, thickness = 0.75 mm) at a temperature of 373 K. The grey cycles represent the experimental data, while red stars represent the result of the fit using the shown model. R_b is the bulk resistance, while CPE_b and CPE_{el} represent the constant-phase elements for the subdiffusive transport and the electrode polarisation, respectively. C_b represents the high-frequency polarization.

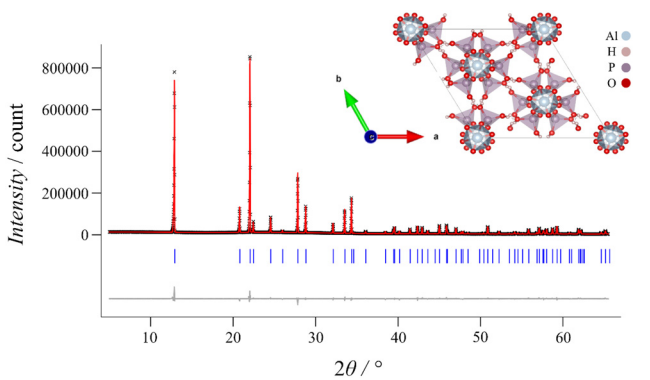

Fig. 2 Rietveld refinement of X-ray diffraction data of C-type Al $(H_2PO_4)_3$ obtained with Cu $K\alpha_1$ radiation (λ = 1.54056 Å) in Debye–Scherrer geometry. The experimental data (black x), the refined fit (red line), and the difference profile (grey line) are presented, along with the Bragg reflections (blue line). The refinement yields a weighted profile R-factor R_{wp} of 5.2% and profile R-factor R_p of 3.3%.

The proton conductivity σ of C-type $Al(H_2PO_4)_3$ was determined from the fitted bulk resistance values R_b, at corresponding temperatures, using the expression $\sigma = \frac{d}{R_b A}$, where d and A denote the sample thickness and the cross-sectional area, respectively. The activation energy (Fig. 4) of the macroscopic ionic conductivity was obtained using the given expression; $\sigma \cdot T = a_0 \exp\left(\frac{-E_a}{k_B T}\right)$, where a_0 is the pre-exponential factor, E_a the activation energy, k_B Boltzmann's constant, and T the temperature (Table 4).

The activation energy, conductivity at selected temperatures and corresponding pre-exponential factor for C-type Al $(H_2PO_4)_3$ are summarised in Table 3. Repeated measurements (Fig. S8 and Table S2) show a minimal variation thereby confirming data reproducibility. The conductivity obtained in this work at 453 K is an order of magnitude higher than the previously reported value at 473 K for C-type $Al(H_2PO_4)_3$.[25] This

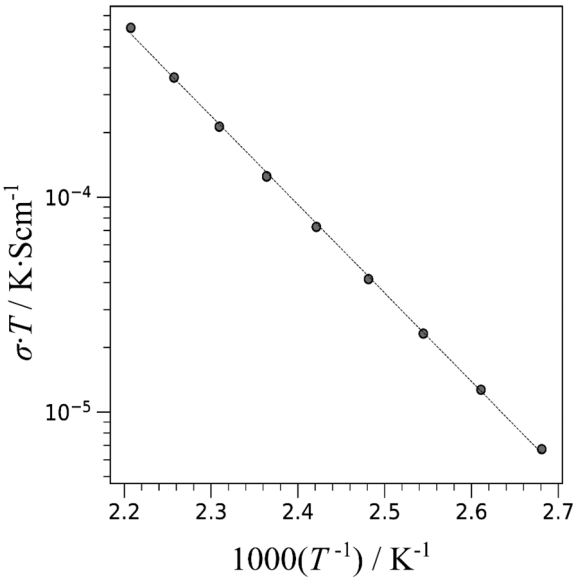

Fig. 4 Plot of the product of electrical conductivity σ and temperature T *versus* inverse temperature for C-type $Al(H_2PO_4)_3$. The results were obtained from impedance spectra in temperature range from 373 K to 453 K (circle). A linear fit which provided the activation energy is indicated by the dashed line.

improvement is attributed to the higher purity of C-type Al $(H_2PO_4)_3$ synthesised in this work. Despite this improvement, the conductivity is still significantly lower than that of *ortho*-phosphoric acid,[50] even though both materials exhibit similar highly polarisable hydrogen-bonds networks. Second moment analysis of C-type $Al(H_2PO_4)_3$ from ^{1}H NMR measurements conducted between 300 K to 453 K (Fig. S9) reveals a strong dipolar coupling. The second moment remains nearly constant up to 453 K, the upper limit of impedance spectroscopy measurements. This invariance indicates minimal motional averaging of the dipolar coupling constant as the sample is thermally activated, implying that the proton dynamics are slow on the NMR timescale within this temperature range. These findings align with the high activation energy obtained from impedance spectroscopy, further showing that pure C-type $Al(H_2PO_4)_3$ is not suitable as an electrolyte for intermediate-temperature fuel cells.[9]

Table 4 The macroscopic conductivity of C-type $Al(H_2PO_4)_3$ at 373 K and 453 K, pre-exponential factor a_0 and the activation energy E_a

	C-type $Al(H_2PO_4)_3$
$\sigma_{373\ K}$/(S cm^{-1})	$1.68(4) \times 10^{-8}$
$\sigma_{453\ K}$/(S cm^{-1})	$1.23(3) \times 10^{-6}$
a_0/(S K cm^{-1})	558168(1)
E_a/eV	0.81(1)

Thermal evolution of C-type $Al(H_2PO_4)_3$

The thermal evolution of phase-pure C-type $Al(H_2PO_4)_3$ was studied over a temperature range of 303–1423 K using thermogravimetric analysis (TGA) and differential thermal analysis (DTA). The DTA curve (Fig. 5) reveals two distinct thermal events: an endothermic event with an onset at 502 K (P_1) and an exothermic event with an onset at 821 K (P_2). The TGA curve indicates that C-type $Al(H_2PO_4)_3$ remains stable up to 512 K (point *a*), after which several mass loss events occur.

The first step, up to point *b* (Fig. 5) is associated with mass loss of 9.1% which corresponds to the condensation of C-type $Al(H_2PO_4)_3$ to an amorphous "$AlH_2P_3O_{10}{\cdot}xH_2O$" ($x \sim 0.4$).

$$Al(H_2PO_4)_3 \rightarrow \text{“}AlH_2P_3O_{10} \cdot xH_2O\text{”} + (2-x)H_2O \qquad (2)$$

Between points *b* and *c* (86%), a gradual mass loss can be observed, which can be interpreted as a continuous loss of

Table 3 C-type $Al(H_2PO_4)_3$ at room temperature obtained from Rietveld refinement of X-ray powder data (λ = 1.54056 Å), as well as the crystallographic data (atomic coordinates *x*, *y*, *z*, displacement parameters B_{eq} and occupancy) of the refined model

	Predicted structural model	Refined structural model
a/Å	13.7111	13.6862(1)
b/Å	13.7111	13.6862(1)
c/Å	9.1477	9.1333(1)
Crystal system	Hexagonal	Hexagonal
Space group	*R*3*c* (no. 161)	*R*3*c* (no. 161)
Z	6	6

Atom	Wyckoff site	*x*	*y*	*z*	Occ.	B_{eq}/Å^2
Al1	6*a*	0	0	0	1	0.61(8)
P1	18*b*	0.0033(3)	0.1623(2)	0.2656(9)	1	1.24(5)
O1	18*b*	0.0340(5)	0.1271(5)	0.3998(9)	1	0.83(5)
O2	18*b*	0.5811(3)	0.5354(3)	0.6204(9)	1	0.83(5)
O3	18*b*	0.4512(3)	0.5045(3)	0.3784(8)	1	0.83(5)
O4	18*b*	0.1251(5)	0.0307(5)	0.1256(9)	1	0.83(5)
H1	18*b*	0.4967(2)	0.5153(2)	0.4631(6)	1	1.24(7)
H2	18*b*	0.5506(2)	0.5401(2)	0.7123(6)	1	1.24(7)

Fit residuals R_{wp} = 5.2%, and R_p = 3.3%. The proton positions were obtained by forcing the H atoms onto the internuclear connectivity vector between the neighbouring O atoms.

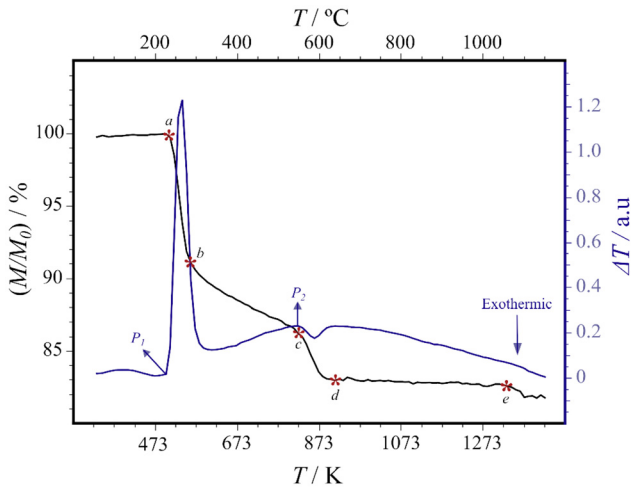

Fig. 5 Thermogravimetric analysis (TGA) (black line) and differential thermal analysis (DTA) (purple line) curves of $Al(H_2PO_4)_3$ recorded over the temperature range of 303 K to 1423 K. The DTA curve shows two thermal events, an endothermic process with onset temperatures at 502 K (P_1) and an exothermic process with onset temperature at 821 K (P_2). The TG curve shows three onset temperatures at *a*, *c*, and *e* which correspond to 512 K, 830 K, and 1324 K, respectively.

water and the formation of amorphous "$AlH_2P_3O_{10}$", theoretically corresponding to a ratio $\Delta M/M_0$ of 88.7%, which is in good agreement with the experiment. The observed mass ratio is a little bit too low, which indicates that the consecutive condensation process has partially started before point *c*, which, for an amorphous material, is not unexpected. Point *c* (TG) and P_2 (DTA) mark the onset at which amorphous "$AlH_2P_3O_{10}$" transforms in an exothermic event by condensation and crystallisation into monoclinic $Al_2(P_6O_{18})$. The observed $\Delta M/M_0$ ratio agrees well with the expected value of 83.0%.

$$2\text{“}AlH_2P_3O_{10}\text{”} \rightarrow Al_2(P_6O_{18}) + 2H_2O \quad (3)$$

The last thermal event at the highest temperature occurs at point *e* (onset at 1324 K). Given that water has already been completely released at lower temperatures, this can only be interpreted as a decomposition reaction involving the release of P_4O_{10}. The formation of $AlPO_4$ would correspond to a mass ratio $\Delta M/M_0$ of 38.4% which does not explain the last step. Cubic $Al_4(P_4O_{12})_3$ is expected to form from monoclinic $Al_2(P_6O_{18})$ in an exothermic event around 1073 K,[17,22] but apparently the effect was below the detection limit.

To confirm this interpretation, NMR and XRD experiments were performed on selected compounds annealed at specific temperatures. In ^{31}P MAS NMR, crystalline and amorphous constituents can be easily identified and quantified: sharp peaks reflect a highly ordered crystal structure, broad peaks reflect the bond-length and bond-angle distribution describing an amorphous material. The ^{31}P and ^{27}Al NMR spectra (Fig. 6) confirm the previous interpretation. An amorphous phase is observed for samples annealed at 573 K and 623 K. The latter already shows a small quantity of the peaks of monoclinic $Al_2(P_6O_{18})$, which is also in line with the TG experiments presented above. The peaks of crystalline phases $AlPO_4$, cubic $Al_4(P_4O_{12})_3$ and monoclinic $Al_2(P_6O_{18})$ were unambiguously identified by their X-ray patterns in agreement with the assignment used in literature.[51–53] Typical for ^{31}P NMR is a correlation between the isotropic chemical shift and the number *n* of bridging O atoms per P atom, which defines the Q^n labels.[54] Bridging here refers to bridging to another P atom, however, it is known that the correlation is further influenced by other factors, including "bridges" to other types of atoms like Al and H, so that a partial overlap between the chemical shift ranges of the Q^n(^{31}P) units results. The correlation of increasing *n* to lower the isotropic chemical shift values is consistent with the isotropic shift of $AlPO_4$ (Q^0), C-type $Al(H_2PO_4)_3$ (Q^0), monoclinic $Al_2(P_6O_{18})$ (Q^2) and cubic $Al_4(P_4O_{12})_3$ (Q^2). The broad ^{31}P peak of the amorphous phase overlaps with the peaks in the Q^2 range, featuring a significant shoulder to higher ppm values, which could be assigned to the presence of Q^1 groups in the amorphous phosphate "$AlH_2P_3O_{10}$". It should be noted that the implicit assumption that the amorphous phosphate corresponds to a triphosphate O_3P-O-PO_2-O-PO_3 is not confirmed by the NMR results. This would require a peak of the Q^1 function being twice as high as the Q^2 peak, which is not observed. A ^{31}P–^{31}P 2D double-quantum MAS NMR spectrum (Fig. 7) of "$AlH_2P_3O_{10}$" shows only a single broad peak and also does not reveal the typical pattern expected for a triphosphate. For this reason, the compound annealed at 573 K most likely should be considered having a composition close to that of the triphosphate $AlH_2P_3O_{10}$, but in reality, it contains a mixture of different chain and ring phosphates. ^{31}P NMR unfortunately does not resolve Q^0, Q^1 and Q^2 peaks to gather further insight. This interpretation is corroborated by the observation of three resolved peaks in ^{27}Al MAS NMR, which by a similar argument can be assigned to 4-, 5- and 6-fold coordinated Al-atoms.

The sample annealed at a temperature of 823 K shows that thermal decomposition of phase-pure C-type $Al(H_2PO_4)_3$ opens a way to the synthesis of phase-pure monoclinic $Al_2(P_6O_{18})$. No impurities could be observed in ^{27}Al and ^{31}P NMR nor in XRD, while in previous studies starting from mixtures of C-type $Al(H_2PO_4)_3$ and H_3PO_4, only heterogeneous mixtures of monoclinic $Al_2(P_6O_{18})$ with additional phases could be observed.[17,22–24] This may open a way to samples doped with different luminescent ions in the host structure $Al_2(P_6O_{18})$ and their unambiguous characterisation. The XRD pattern of monoclinic $Al_2(P_6O_{18})$ (Fig. S10),[52] its ^{31}P and ^{27}Al NMR parameters of the different sites determined from fitting NMR spectra (Fig. S5) and a ^{31}P 2D double-quantum MAS NMR (Fig. S11) are shown in the SI and Tables 1 and 2.

NMR and XRD on a sample annealed at a temperature of 1273 K show that monoclinic $Al_2(P_6O_{18})$ has converted into cubic $Al_4(P_4O_{12})_3$ and a small trace of $AlPO_4$ (Fig. 6). In an attempt to remove the impurity of $AlPO_4$, phase-pure C-type $Al(H_2PO_4)_3$ was annealed at a temperature of 1273 K in a vacuum of $\sim 10^{-2}$ mbar for 6 and 24 hours, respectively, assuming that the formed small quantity of $AlPO_4$ could be related to a surface coverage by OH functions. Surprisingly, the product of

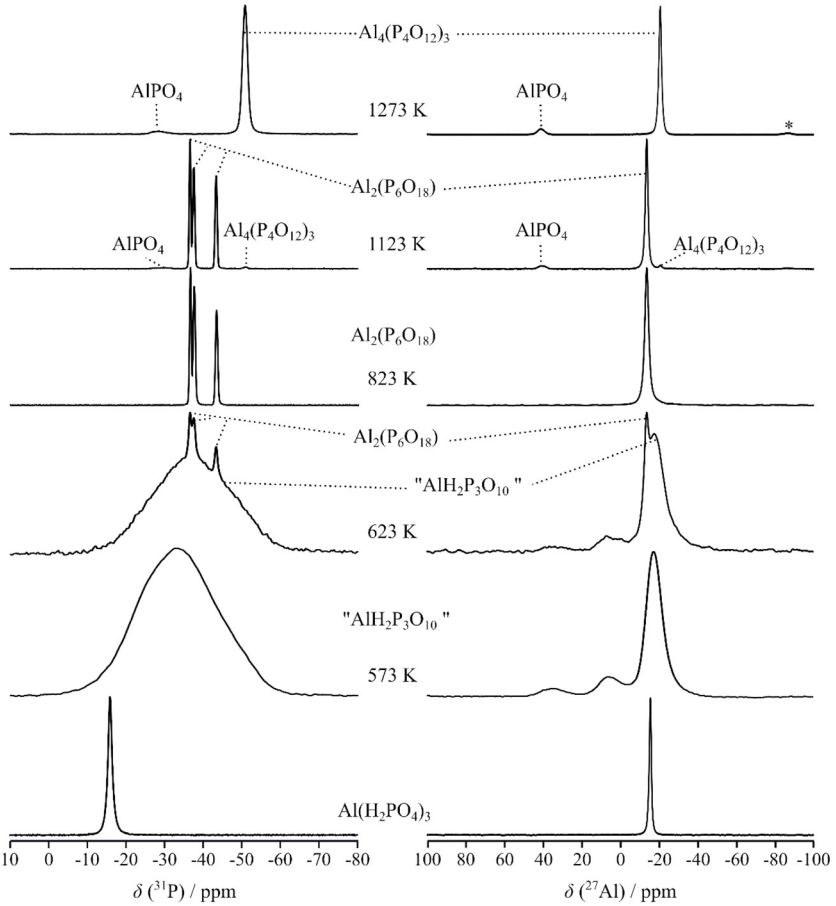

Fig. 6 ^{31}P and ^{27}Al MAS NMR single-pulse measurements of C-type $Al(H_2PO_4)_3$ and its thermal decomposition products obtained at different annealing temperatures measured at 20 kHz spinning frequency showing the isotropic signals and * as the spinning side band of $AlPO_4$. The repetition delays were chosen longer than $5T_1$.

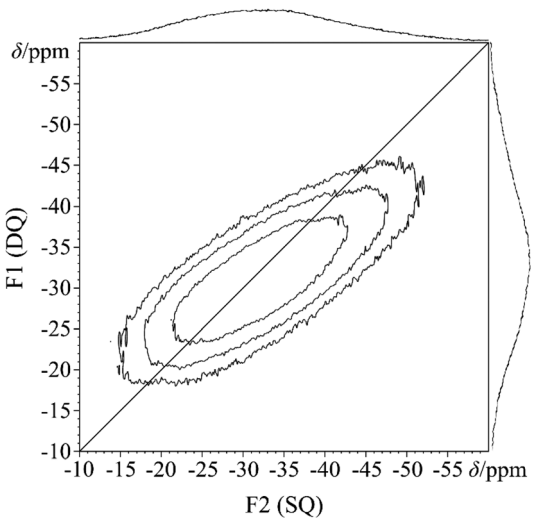

Fig. 7 The ^{31}P–^{31}P 2D double-quantum NMR spectrum of "$AlH_2P_3O_{10}$" annealed at 573 K, acquired at a spinning frequency of 20 kHz, shows a broad phosphorus peak in the double-quantum dimension. The indirect dimension is scaled such that DQ signals of isochronous pairs are on the diagonal.

this attempt at 6 hours was mixture of $Al_2(P_6O_{18})$, $Al_4(P_4O_{12})_3$, and $AlPO_4$ while the product of the attempt at 24 hours produces only $AlPO_4$ (NMR and XRD not shown), which proves that the phase transitions are catalysed by small quantities of the remaining water, which indicates that the transition temperatures of the crystallisation of the amorphous phase observed in thermal analysis may be difficult to reproduce without knowing the partial pressure of water.

For cubic $Al_4(P_4O_{12})_3$, the crystal structure published in the year 1937 [53] provides the correct position of reflections but an unsatisfactory match of the intensities (Fig. S13). NMR spectra resolve one P and one Al site, with chemical shift tensors obtained from Fig. S6 spectra listed in Tables 1 and 2. This indicates that the published structure is correct, but the atomic positions could be improved by a Rietveld refinement. For this purpose, the structure for the substituted variant $(Al_{3.39}V_{0.61})(P_4O_{12})_3$,[55] determined by single-crystal X-ray diffraction, was taken as a starting point. The refined structure is in excellent agreement with the powder XRD with cubic lattice parameters of a = 13.735(2) Å (Fig. S12 and Table S3). Furthermore, the structure obtained from Rietveld refinement was converted to $P1$ space group with respect to the fractional

coordinates of the atoms and was relaxed using Quantum Espresso to establish whether the structure corresponds to an energetic minimum. The relaxed structure shows minimal changes, as confirmed by visual inspection and comparison of powder XRD patterns (Fig. S13). The space group also remains $I\bar{4}3d$, as confirmed by KPLOT,[56] validating the new structure for $Al_4(P_4O_{12})_3$, which means that the structure is confirmed through independent evidence by NMR, XRD and quantum-chemical calculations.

Conclusions

The crystallographic data of C-type $Al(H_2PO_4)_3$ were successfully generated, enabling the investigation of the thermodynamic stability of $Al(H_2PO_4)_3$ polymorphs *via* DFT calculations. This study identified C-type $Al(H_2PO_4)_3$ as the most thermodynamically stable polymorph, leading to the first reported synthesis of phase-pure C-type $Al(H_2PO_4)_3$. The enhanced purity of the synthesised compound was shown to improve its proton conductivity and its thermal evolution pathways, thereby providing updated insights into its stability and potential use in high-temperature refractory applications.

Author contributions

Conceptualisation: J. S. A. D. G., C. F. L.; formal analysis: S. C. A., J. K. W., C. F. L.; investigation: S. C. A., J. K. W., C. F. L.; writing – original draft preparation: S. C. A.; writing – reviewing and editing: J. S. A. D. G.; visualisation: S. C. A., J. K. W.; funding acquisition: J. S. A. D. G., S. C. A.; supervision: J. S. A. D. G.

Conflicts of interest

There are no conflicts to declare.

Data availability

The data supporting this article have been included as part of the supplementary information (SI). Supplementary information: solid-state NMR characterisation, Rietveld refinement analysis, electrochemical impedance spectroscopy, and second moment line shape analysis. See DOI: https://doi.org/10.1039/d5dt02141c.

CCDC 2485462 and 2485463 contain the supplementary crystallographic data for this paper.[57a,b]

Acknowledgements

We thank Dr Sergei Ivlev (Philipps-Universität Marburg) and Dr Jörg Daniels (Rheinische Friedrich-Wilhelms-Universität Bonn) for their assistance with XRD measurements. We also thank Prof. Dr Bernhard Roling (Philipps-Universität Marburg) for insightful discussions on the EIS data analysis. Financial support from the House of Young Talents, University of Siegen is acknowledged.

References

1 W. D. Kingery, *J. Am. Ceram. Soc.*, 1950, **33**, 239–241.
2 J. H. Morris, P. G. Perkins, A. E. A. Rose and W. E. Smith, *Chem. Soc. Rev.*, 1977, **6**, 173–194.
3 J.-M. Chiou and D. D. L. Chung, *J. Mater. Sci.*, 1993, **28**, 1435–1446.
4 A. P. Luz, G. R. Oliveira, D. T. Gomes and V. C. Pandolfelli, *Ceram. Int.*, 2016, **42**, 8331–8337.
5 A. P. Luz, D. T. Gomes and V. C. Pandolfelli, *Ceram. Int.*, 2015, **41**, 9041–9050.
6 J. A. Fernando and D. D. L. Chung, *J. Mater. Sci.*, 2001, **36**, 5079–5085.
7 Y. Li, G. Chen, S. Zhu, H. Li, Z. Ma, Y. Liu and L. Liu, *Bull. Mater. Sci.*, 2019, **42**, 200.
8 L. He, D. Chen and S. Shang, *J. Mater. Sci.*, 2004, **39**, 4887–4892.
9 K.-D. Kreuer, *Chem. Mater.*, 1996, **8**, 610–641.
10 L. Giorgi and F. Leccese, *Open Fuel Cells J.*, 2013, **6**, 1–20.
11 Th. Dippel, K. D. Kreuer, J. C. Lassègues and D. Rodriguez, *Solid State Ionics*, 1993, **61**, 41–46.
12 R. Kniep and M. Steffen, *Angew. Chem., Int. Ed. Engl.*, 1978, **17**, 272–273.
13 D. Brodalla, R. Kniep and D. Mootz, *Z. Naturforsch., B: J. Chem. Sci.*, 1981, **36**, 907–909.
14 V. Lyutsko, A. Selevich and T. Romanii, *Russ. J. Inorg. Chem.*, 1989, **34**, 1152–1155.
15 P. Rémy and F. d'Yvoire, *C. R. Hebd. Seances Acad. Sci.*, 1960, **250**, 2213–2215.
16 F. d'Yvoire, *Bull. Soc. Chim. Fr.*, 1961, 2277–2282.
17 G. Tricot, D. Coillot, E. Creton and L. Montagne, *J. Eur. Ceram. Soc.*, 2008, **28**, 1135–1141.
18 N. Belfguira, S. Walha, A. Ben Salah, A. M. Fransolet and A. Kabadou, *Acta Crystallogr., Sect. C: Struct. Chem.*, 2010, **66**, i33–i36.
19 J. Hoja, A. M. Reilly and A. Tkatchenko, *Wiley Interdiscip. Rev.: Comput. Mol. Sci.*, 2017, **7**, e1294.
20 G. Hautier, S. P. Ong, A. Jain, C. J. Moore and G. Ceder, *Phys. Rev. B: Condens. Matter Mater. Phys.*, 2012, **85**, 155208.
21 M. Vippola, J. Vuorinen, P. Vuoristo, T. Lepistö and T. Mäntylä, *J. Eur. Ceram. Soc.*, 2002, **22**, 1937–1946.
22 Q. Wang, D. Jia, W. Duan, H. Yang, S. Ma, P. He, P. Colombo and Y. Zhou, *J. Alloys Compd.*, 2023, **966**, 171487.
23 D. Hahn, A. Masoudi Alavi and P. Quirmbach, *Mater. Chem. Phys.*, 2021, **267**, 124663.
24 G. Rousseau, L. Montagne and F. O. Méar, *J. Eur. Ceram. Soc.*, 2021, **41**, 4970–4976.
25 X. Xu, S. Tao and J. T. S. Irvine, *Solid State Ionics*, 2009, **180**, 343–350.

26 J. Nasir, N. Steinbrück, K. Xu, B. Engelen and J. Schmedt auf der Günne, *J. Appl. Crystallogr.*, 2022, **55**, 1097–1103.
27 A. A. Coelho, *J. Appl. Crystallogr.*, 2018, **51**, 210–218.
28 G. S. Pawley, *J. Appl. Crystallogr.*, 1981, **14**, 357–361.
29 H. M. Rietveld, *J. Appl. Crystallogr.*, 1969, **2**, 65–71.
30 R. K. Harris and E. D. Becker, *J. Magn. Reson.*, 2002, **156**, 323–326.
31 R. K. Harris, E. D. Becker, S. M. Cabral de Menezes, P. Granger, R. E. Hoffman and K. W. Zilm, *Pure Appl. Chem.*, 2008, **80**, 59–84.
32 P. E. Kristiansen, M. Carravetta, J. D. van Beek, W. C. Lai and M. H. Levitt, *J. Chem. Phys.*, 2006, **124**, 234510.
33 D. Jardón-Álvarez and J. Schmedt auf der Günne, *Solid State Nucl. Magn. Reson.*, 2018, **94**, 26–30.
34 M. Bak, J. T. Rasmussen and N. C. Nielsen, *J. Magn. Reson.*, 2000, **147**, 296–330.
35 T. Vosegaard, A. Malmendal and N. C. Nielsen, *Monatsh. Chem.*, 2002, **133**, 1555–1574.
36 S. C. Adediwura, N. Mathew and J. Schmedt auf der Günne, *J. Mater. Chem. A*, 2024, **12**, 15847–15857.
37 P. Giannozzi, S. Baroni, N. Bonini, M. Calandra, R. Car, C. Cavazzoni, D. Ceresoli, G. L. Chiarotti, M. Cococcioni, I. Dabo, A. D. Corso, S. de Gironcoli, S. Fabris, G. Fratesi, R. Gebauer, U. Gerstmann, C. Gougoussis, A. Kokalj, M. Lazzeri, L. Martin-Samos, N. Marzari, F. Mauri, R. Mazzarello, S. Paolini, A. Pasquarello, L. Paulatto, C. Sbraccia, S. Scandolo, G. Sclauzero, A. P. Seitsonen, A. Smogunov, P. Umari and R. M. Wentzcovitch, *J. Phys.: Condens. Matter*, 2009, **21**, 395502.
38 P. Giannozzi, O. Andreussi, T. Brumme, O. Bunau, M. B. Nardelli, M. Calandra, R. Car, C. Cavazzoni, D. Ceresoli, M. Cococcioni, N. Colonna, I. Carnimeo, A. D. Corso, S. de Gironcoli, P. Delugas, R. A. DiStasio, A. Ferretti, A. Floris, G. Fratesi, G. Fugallo, R. Gebauer, U. Gerstmann, F. Giustino, T. Gorni, J. Jia, M. Kawamura, H.-Y. Ko, A. Kokalj, E. Küçükbenli, M. Lazzeri, M. Marsili, N. Marzari, F. Mauri, N. L. Nguyen, H.-V. Nguyen, A. Otero-de-la-Roza, L. Paulatto, S. Poncé, D. Rocca, R. Sabatini, B. Santra, M. Schlipf, A. P. Seitsonen, A. Smogunov, I. Timrov, T. Thonhauser, P. Umari, N. Vast, X. Wu and S. Baroni, *J. Phys.: Condens. Matter*, 2017, **29**, 465901.
39 J. P. Perdew, K. Burke and M. Ernzerhof, *Phys. Rev. Lett.*, 1996, **77**, 3865–3868.
40 D. C. Langreth, B. I. Lundqvist, S. D. Chakarova-Käck, V. R. Cooper, M. Dion, P. Hyldgaard, A. Kelkkanen, J. Kleis, L. Kong, S. Li, P. G. Moses, E. Murray, A. Puzder, H. Rydberg, E. Schröder and T. Thonhauser, *J. Phys.: Condens. Matter*, 2009, **21**, 084203.
41 K. Berland, V. R. Cooper, K. Lee, E. Schröder, T. Thonhauser, P. Hyldgaard and B. I. Lundqvist, *Rep. Prog. Phys.*, 2015, **78**, 066501.
42 T. Thonhauser, V. R. Cooper, S. Li, A. Puzder, P. Hyldgaard and D. C. Langreth, *Phys. Rev. B: Condens. Matter Mater. Phys.*, 2007, **76**, 125112.
43 T. Thonhauser, S. Zuluaga, C. A. Arter, K. Berland, E. Schröder and P. Hyldgaard, *Phys. Rev. Lett.*, 2015, **115**, 136402.
44 G. Kresse and D. Joubert, *Phys. Rev. B: Condens. Matter Mater. Phys.*, 1999, **59**, 1758–1775.
45 H. J. Monkhorst and J. D. Pack, *Phys. Rev. B*, 1976, **13**, 5188–5192.
46 A. Dal Corso, *Comput. Mater. Sci.*, 2014, **95**, 337–350.
47 T. Björkman, *Comput. Phys. Commun.*, 2011, **182**, 1183–1186.
48 D. Müller, E. Jahn, G. Ladwig and U. Haubenreisser, *Chem. Phys. Lett.*, 1984, **109**, 332–336.
49 D. Damjanovic, *Rep. Prog. Phys.*, 1998, **61**, 1267.
50 Y. Aihara, A. Sonai, M. Hattori and K. Hayamizu, *J. Phys. Chem. B*, 2006, **110**, 24999–25006.
51 H. N. Ng and C. Calvo, *Can. J. Phys.*, 1976, **54**, 638–647.
52 A. Oudahmane, A. Mbarek, M. El-Ghozzi and D. Avignant, *Acta Crystallogr., Sect. E: Crystallogr. Commun.*, 2010, **66**, i17–i17.
53 L. Pauling and J. Sherman, *Z. Kristallogr. – Cryst. Mater.*, 1937, **96**, 481–487.
54 E. Lippmaa, M. Maegi, A. Samoson, G. Engelhardt and A. R. Grimmer, *J. Am. Chem. Soc.*, 1980, **102**, 4889–4893.
55 O. V. Yakubovich, G. V. Biralo and O. V. Dimitrova, *Crystallogr. Rep.*, 2012, **57**, 193–199.
56 R. Hundt, *KPLOT A Program for Plotting and Analysing Crystal Structures, Version 9*, Technicum Scientific Publishing, Stuttgart, 2016.
57 (*a*) CCDC 2485462: Experimental Crystal Structure Determination, 2025, DOI: 10.5517/ccdc.csd.cc2pfb6p; (*b*) CCDC 2485463: Experimental Crystal Structure Determination, 2025, DOI: 10.5517/ccdc.csd.cc2pfb7q.